Flight Dynamics Conceptual Design Exploration of Multirotor eVTOL

Carlos Malpica
Aerospace Engineer
Aeromechanics Branch
NASA Ames Research Center
Moffett Field, CA, USA

Peter Suh
Aerospace Engineer
Flight Controls & Dynamics Branch
NASA Armstrong Flight Research Center
Edwards, CA, USA

Christopher Silva
Aerospace Engineer
Aeromechanics Branch
NASA Ames Research Center
Moffett Field, CA, USA

ABSTRACT

The advent of electric propulsion is revolutionizing the paradigm of rotorcraft design, leading to new electric Vertical Take-Off and Landing (eVTOL) aircraft. Direct drive topologies are common within these new designs, and some designers have chosen to utilize this mechanism for Primary Flight Control (PFC), effectively utilizing the aircraft engines as PFC actuators to control the speed of the rotors. This decision integrates the propulsion and flight control systems, and intrinsically couples the aircraft sizing and control. Four separate tools were exercised throughout this study to conduct a conceptual design exploration of eVTOL aircraft handling qualities. The main tasks for these tools were: 1) aircraft sizing and performance analysis, including the calculation of trim; 2) flight dynamics modeling and analysis; 3) handling qualities-centric control law optimization; and 4) electric motor sizing. Sizing of an RPM-controlled Hexacopter concept explored the dependency of aircraft size to fundamental design parameters: 1) disk loading and 2) blade loading coefficient. Increasing the design disk loading resulted in designs with high agility, but at the cost of significant growth in the design gross weight. Finally, Categories II and III pilot-induced-oscillation (PIO) are known potentially-catastrophic handling qualities deficiencies of fly-by-wire flight control systems such as those expected of eVTOL aircraft. Consideration of PIO predictive metrics in conceptual design control synthesis led to increased PIO robustness.

NOTATION

Symbols

A_{ref}	Total rotor disk (reference) area (ft^2)
A	Linear state-space model stability matrix
B	Linear state-space model control matrix
$c_{i,\text{input}}$	Control allocation mixing coefficient
c_μ	Motor viscous damping coefficient
C_W/σ	Design blade loading, $W_D/\rho A_{\text{ref}} V_{tip}^2 \sigma$
$\mathbf{C}(s)$	MIMO command model matrix
f_P	Fraction of power available for sizing
G_{inv}	Inverter voltage output gain
G_r	Powertrain transmission gear ratio
$\mathbf{G}(s)$	Aircraft transfer matrix with rotor speed control
$\mathbf{G}_a(s)$	Bare-airframe aircraft transfer matrix
$\mathbf{H}(s)$	Inner-loop MIMO feedback regulator matrix
$\mathbf{H}_\Omega(s)$	Rotor speed controller feedback matrix
I_d, I_q	Motor stator D- and Q-axis currents (A)
I_{xx}, I_{yy}, I_{zz}	Aircraft principal moments of inertia ($\text{slug}\cdot\text{ft}^2$)
I_R	Rotor moment of inertia ($\text{slug}\cdot\text{ft}^2$)
k_x, k_y, k_z	Normalized aircraft radii of gyration
$\mathbf{L}(s)$	Low-order transfer function approximation of $\mathbf{G}(s)$
L_d, L_q	Motor rotor D- and Q-axis self-inductances (mH)
L_p, L_{Q_i}	Roll damping and torque control derivatives
m	Aircraft mass (slug)
M	Motor modulation ratio
M_q, M_{Q_i}	Pitch damping and torque control derivatives
n_c	Number of aircraft components
n_p	Number of motor pole pairs
n_r	Number of rotors
N_r, N_{Q_i}	Yaw damping and torque control derivatives
p	Body x-axis angular rate (rad/s)
P_{av}	Power available per engine group (hp or kW)
P_H	Motor power heat losses (hp or kW)
P_I	Motor active, or input, electrical power (hp or kW)
P_L	Motor load power (hp or kW)
P_{eng}	Max. power available per engine group (hp or kW)
P_{req}	Power required per engine group (hp or kW)
q	Body y-axis angular rate (rad/s)
Q	Rotor aerodynamic torque ($\text{ft}\cdot\text{lb}$)
Q_0	Rotor trim torque ($\text{ft}\cdot\text{lb}$)
Q_M	Rotor shaft torque margin ($\text{ft}\cdot\text{lb}$)
Q_{peak}	Mechanical torque limit of motor ($\text{ft}\cdot\text{lb}$ or $\text{N}\,\text{m}$)
Q_S	Rotor shaft torque ($\text{ft}\cdot\text{lb}$)
$\hat{Q}_{\text{input}}$	Input-aligned torque command (non-dimensional)
r	Body z-axis angular rate (rad/s)
R	Rotor radius (ft)
R_s	Motor stator resistance (Ω)
R_s^{25}	Motor stator resistance measured at 25 °C (Ω)
$\mathbf{S}(s)$	Feedback sensor transfer functions
T	Rotor thrust (lb)
T_{DN}	NDARC drivetrain control allocation matrix
$\mathbf{u}_a$	Aircraft inputs (i.e., rotor speed commands)
$\boldsymbol{u}$	Linear state-space model input vector

Presented at the Vertical Flight Society's 80th Annual Forum & Technology Display, Montréal, Québec, Canada, May 7–9, 2024.

$\boldsymbol{u}_{c_i}$	Input vector from i-th aircraft component
V_b	DC-voltage measured at inverter terminal (V)
V_{be}	Speed for best endurance (knot)
V_{br}	Speed for best range (knot)
V_d, V_q	Motor steady state D- and Q-axis stator voltages (V)
V_m	Motor battery voltage (V)
V_{max}	Maximum speed (knot)
V_s	Motor stator voltage (V)
V_{tip}	Rotor hover tip speed, given by ΩR (ft/s)
w	Body z-axis velocity (ft/s)
W_D	Design gross weight (lb)
$\boldsymbol{x}$	Linear state-space model state vector
$\mathbf{y}$	Aircraft response vector
Z_w, Z_{Q_i}	Heave damping and torque control derivatives
α	Motor voltage angle (rad)
α_{pm}	Permanent magnet thermal coefficient (1/°C)
α_c	Copper thermal coefficient (1/°C)
β	Rotor blade flapping angle (deg or rad)
$\beta_0, \beta_{1c}, \beta_{1s}$	Rotor coning and tilt degrees of freedom (deg or rad)
δ	Motor current angle (rad)
$\boldsymbol{\delta}$	Vector of pilot inputs
η_m	Motor power conversion efficiency
λ	Motor flux linkage (Wb)
$\lambda_0, \lambda_{1c}, \lambda_{1s}$	Dynamic inflow states
λ^{20}	Motor flux linkage measured at 20 °C (Wb)
σ	Rotor thrust-weighted solidity
τ_e	Command model equivalent time delay (s)
τ_h	Motor hysteresis friction loss (ft · lb or N m)
τ_l	Motor viscous torque losses (ft · lb or N m)
τ_L	Motor load torque (ft · lb or N m)
θ_r	Average temperature of motor permanent magnets (°C)
θ_w	Average temperature of motor winding (°C)
Φ	Motor power factor
ω_m	Motor speed (rad/s)
Ω	Rotor speed (rad/s)
Ω_0	Trim rotor speed (rad/s)
Ω_i	Rotor speed for i-th rotor (rad/s)
Ω_M	Rotor speed margin (rpm or rad/s)

Superscripts

b	Motor base condition
r	Motor rated condition
p	Motor peak value

Key Acronyms

ACAH	Attitude Command-Attitude Hold
BLDC	Brushless Direct Current
DGW	Design Gross Weight
DRB	Disturbance Rejection Bandwidth
DRP	Disturbance Rejection Peak
eVTOL	electric Vertical Take-Off and Landing
EMC	Electric Motor Controller
FW	Flux Weakening
MCP	Maximum Continuous Power
MCT	Maximum Continuous Torque
MRP	Maximum Rated Power
MTOW	Maximum Take-Off Weight
NFW	No-Flux Weakening
OLOP	Open-Loop Onset Point
PFC	Primary Flight Control
PMSM	Permanent Magnet Synchronous Motor
RCDH	Rate Command-Direction Hold
RCHH	Rate Command-Height Hold
RSC	Rotor Speed Controller

INTRODUCTION

The advent of electric propulsion is revolutionizing the paradigm of rotorcraft design. New, emerging, electric Vertical Take-Off and Landing (eVTOL) aircraft offer a potentially revolutionary new form of transportation, if certain technical shortcomings are to be resolved (Refs. 1, 2). Industry, while advancing quite rapidly, is not yet free from the expensive cycle of technology prototyping. Joby Aviation, to pick one, went through the Monarch and the S2, before arriving at the S4 (of which there have been various prototype variants). Wisk Aero has gone through at least five generations (as Zee Aero and Kitty Hawk) before arriving at their Cora prototype; a Generation 6 has now been announced. Archer Aviation built the 80%-scale technology demonstrator Maker before rollout of their Midnight production prototype, although these efforts were almost in parallel. Vertical Aerospace, in the United Kingdom, built the VA-X1 and VA-X2 prototypes before pivoting aircraft type and developing the VX4 production model.

This is potentially indicative of either the inadequacy of early design tools, or of tools not being adopted. To address the former, NASA developed the NASA Design and Analysis of Rotorcraft (NDARC) software (Ref. 3), which allows the sizing and analysis of rotorcraft configurations based on mission performance requirements and technology assumptions. Flight dynamics, but more specifically the handling qualities of aircraft, have historically not been considered at the conceptual design level (Refs. 4, 5). The framework of Ref. 5 was proposed as a means of addressing this gap, as a partner tool to NDARC. Recently, some work in the area has recognized this need as well (Refs. 6–8).

Commonly, many of these new configurations tend to have large numbers of lifting rotors (typically between four and twelve) compared to conventional rotorcraft, with each rotor usually driven by its own independent propulsion system, in a topology often referred to as Distributed Electric Propulsion (DEP). Although not true to every configuration, some designers have chosen to utilize the DEP mechanism for Primary Flight Control (PFC), effectively utilizing the aircraft engines as PFC actuators to control the speed of the rotors. Crucially, this decision integrates the propulsion and flight control systems, and intrinsically couples the aircraft sizing and control.

The objectives of this study are to investigate connections between conceptual design sizing parameters and the flight dy-

namics of eVTOL aircraft. Specifically, the paper will explore how design parameters affect the control and maneuverability of DEP aircraft in low speed, rotor-borne flight. A sensitivity analysis is conducted at the conceptual design level, utilizing NDARC to size the aircraft. A flight dynamics analysis is then conducted for every design iteration to assess variations in the bare-airframe dynamics, firstly, and the effect of actuator size when an optimal flight control system is synthesized to satisfy explicit handling qualities requirements, secondly.

METHODOLOGY

Vehicle Sizing

Vehicle sizing is one of the defining tasks of conceptual design, where fundamental aspects such as fuselage shape, wing and rotor configuration and location, engine size and type that satisfactorily meet all specified requirements look to be determined. This is a multidisciplinary process that must consider several oft-competing factors in aerodynamics, propulsion, flight performance, structures and control systems (Refs. 4,9). The NASA Design and Analysis of Rotorcraft (NDARC) software helps manage many of these competing requirements and was utilized to size the aircraft and to conduct parameter trade studies of interest.

Following a component-based approach, NDARC relies on low-fidelity models typically appropriate for the conceptual design environment to represent the power and energy transfer between components, the aerodynamic (or other) forces and moments produced by components, component weight, etc. to characterize the aircraft design as a whole. NDARC iteratively solves for the vehicle dimensions, power and weight given a prescribed set of design conditions and/or missions. For this study, a set of mission requirements representative of Urban Air Mobility (UAM) operations from Ref. 2 was utilized for the aircraft sizing (see Table 1 and Figure 1). From these requirements NDARC can determine the total engine power and the rotor radius for each propulsion group, as well as the design gross weight, maximum takeoff weight, drive system torque limit, and fuel tank capacity.

Previous studies (Refs. 10–12) progressively explored some of the limitations of RPM control. Ref. 13, in particular, provided powerful insight into the torque margins required from the engine group to ensure acceptable handling qualities. The sizing of the engine power for eVTOL, and specifically for eVTOL using rotor speed as the primary means of control, was thus of critical interest in this study.

The motor size in NDARC is defined by the maximum power available P_{eng} and a peak torque limit Q_{peak} representing the mechanical limit of the motor, such that power available is given by

$$P_{av} = \begin{cases} f_P \omega_m Q_{\text{peak}}, & \omega_m < \omega_m^b \\ f_P P_{\text{eng}}, & \omega_m \geq \omega_m^b \end{cases} \tag{1}$$

where ω_m^b is the base speed of the motor, i.e., the speed at which both power available and torque limits coincide. Note that Eq. 1 denotes a fundamental physical relationship, and that proper bookkeeping of units is needed, especially when dealing with non-SI units.

The fraction of power available f_P is a means of allocating a certain amount of power to the sizing task, effectively building in power margins into the engine size. When sizing, power available P_{av} is fundamentally set by the power required P_{req}, i.e., $P_{av} = P_{req}$, from the different sizing conditions. From Eq. 1 it then follows, e.g., that

$$P_{\text{eng}} = \frac{1}{f_P} P_{req} \tag{2}$$

such that $P_{\text{eng}} > P_{req}$ for $f_P < 1$.

It is noted that NDARC does not limit the motor speed ω_m in any fundamental way, but the ratio of the maximum power to the torque limit for each motor rating, and thus the base speed, is an input parameter into NDARC. So is the ratio of maximum power to continuous power ratings (MRP/MCP).

Handling Qualities

A framework for including handling qualities in conceptual design of rotorcraft was first proposed in Ref. 5. The processes applicable to the assessment of RPM-control handling qualities have been progressively matured through analysis (Refs. 10–12) and experimental validation (Ref. 13). Key processes are now being implemented into the new rotorcraft Flight dynamics and control modeling and analysis tool for COnceptual DEsign (FlightCODE). FlightCODE envisions improvements in terms of computational efficiency and capabilities over the framework of Ref. 5. New features (Refs. 14,15) and uses (Ref. 16) are currently in development. The features directly relevant to this study are summarized in the following sections.

Linear models The core capability of FlightCODE lies in the rapid generation of linear perturbation stability and control derivative models of the NDARC-sized aircraft designs. Models generated are in the general state-space form

$$\begin{bmatrix} \dot{\boldsymbol{x}}_b \\ \dot{\boldsymbol{x}}_\beta \\ \dot{\boldsymbol{x}}_\lambda \\ \dot{\boldsymbol{x}}_r \end{bmatrix} = A \begin{bmatrix} \boldsymbol{x}_b \\ \boldsymbol{x}_\beta \\ \boldsymbol{x}_\lambda \\ \boldsymbol{x}_r \end{bmatrix} + B \begin{bmatrix} \boldsymbol{u}_{c_1} \\ \boldsymbol{u}_{c_2} \\ \vdots \\ \boldsymbol{u}_{c_{n_c}} \end{bmatrix} \tag{3}$$

where state vectors $\boldsymbol{x}_b, \boldsymbol{x}_\beta, \boldsymbol{x}_\lambda$ and $\boldsymbol{x}_r$ include the aircraft rigid body translational and rotational degrees of freedom, rotor flapping degrees of freedom for each rotor, 3-state dynamic inflow states for each wake, and rotational degrees of freedom of each rotor, respectively, and the input vectors $\boldsymbol{u}_{c_i}$ correspond to the control effector inputs associated with the i-th aircraft component. The specific definition of the control inputs, as well as a default control allocation matrix mapping the four main aircraft controls to the component controls, are inherited from NDARC.

Table 1. Sizing mission segments and their associated properties.

Segments	1&10	2&11	3&12	4&13	5&14	6&15	7&16	8&17	9&18	19
Initial Alt. (MSL ISA)	6,000	6,000	6,050	6,050	10,000	6,050	6,050	6,050	6,000	10,000
Final Alt. (MSL ISA)	6,000	6,050	6,050	10,000	10,000	6,050	6,050	6,000	6,000	10,000
Time (s)	15	30	10	t_{climb}	t_{cruise}	10	30	30	15	1,200
Distance (nmi)	–	0	0	D_{climb}	$37.5 - D_{climb}$	0	0	0	0	–
Speed	–	–	0	V_x	V_{br}	0	0	–	–	V_{be}
ROC (ft/min)	–	100	0	$\geq$900	0	0	0	-100	–	0
Percent of Max Power	10%	100%	100%	P_{climb}	P_{cruise}	100%	100%	100%	10%	P_{cruise}

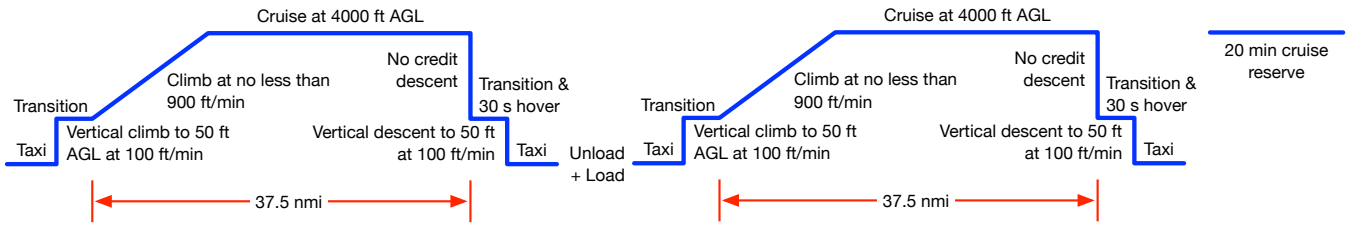

Figure 1. Sizing mission profile.

For conventional rotorcraft, component controls typically consist of the rotor collective and cyclic inputs, and in some instances, airframe aerodynamic control surfaces. For aircraft using rotor speed as the primary means of control, it was necessary to model the rotational dynamics of the rotor. Inputs were defined by setting

$$\boldsymbol{u}_{c_i} = Q_{S_i} \quad \text{for} \quad i = 1, 2, \cdots n_r$$

where Q_{S_i} are the torques to the rotor shafts and n_r is the number of rotors.

The rotor blades are assumed rigid, with a hinge offset and spring stiffness implemented to match the fundamental flapping frequency from NDARC. The second-order linear perturbation equations for the flap motion in the non-rotating frame are symbolically generated and coded for computational expediency, with the coning β_0 and tip-path-plane tilt β_{1s} and β_{1c} degrees of freedom modeled for each rotor. The coupled nature of the rotor-airframe dynamics is formally retained, with shaft motion being accounted for in the flap equations of motion. The dynamic inflow formulation in the tool follows from the perturbation version of the generalized Peters-HaQuang model (Ref. 17). The finite-state wake model considers only the uniform, lateral and longitudinal variations in rotor inflow, denoted by λ_0, λ_{1s} and λ_{1c}, respectively.

Flight dynamics assessment Historical approaches to the treatment of stability and control during conceptual design are limited to basic sizing and placement of wings and aerodynamic control surfaces to guarantee adequate stability (static and dynamic) and trim, while handling qualities are typically deferred to later stages of design (Ref. 4). Rotorcraft introduce added complication in that these types of aircraft are often inherently unstable. Also, the methods for estimating the rotor dynamics effects are somewhat more involved than those employed for fixed-wing aircraft.

Developments in flight control technology suggest that fly-by-wire systems with increased stability augmentation and advanced control modes to reduce pilot workload will be increasingly more prevalent. It can in fact safely be assumed that new eVTOL aircraft will by default be equipped with fly-by-wire systems and highly augmented controls. These systems tend to shift the handling qualities burden away from the bare-airframe design and onto the flight control system design, provided the actuators possess sufficient control authority. Fly-by-wire systems present new types of handling qualities deficiencies and certification challenges, however. In particular, real concerns exist about the potential for severe Category II or III pilot induced oscillations (PIO) that can develop with fly-by-wire controls (Ref. 18). Causes vary, but a key trigger of these types of severe PIO is linked to the onset of nonlinearities in the aircraft dynamics, such as those associated with actuator rate limiting.

These issues raise questions about the best approach for assessing the controllability and maneuverability or the handling qualities at the conceptual stage of design. The answer lies possibly in the implementation of a flexible analysis framework that enables both classical stability and control assessments, and a more modern handling qualities-centric analytical approach. It is observed that the linear models of Eq. 3 can support both types of analysis and that trimmability assessment can be conducted using NDARC. The classical approach would be informed by the open-loop bare-airframe stability and control characteristics determined from Eq. 3. When considering the handling qualities of highly-augmented systems it is arguably unavoidable to consider the effect of feedback stabilization and control response mode shaping. The ultimate goal, however, should be to quantify the required system control authority so as to provide actionable information that can be used to adequately size the actuators.

An explicit model-following control system architecture (Fig-

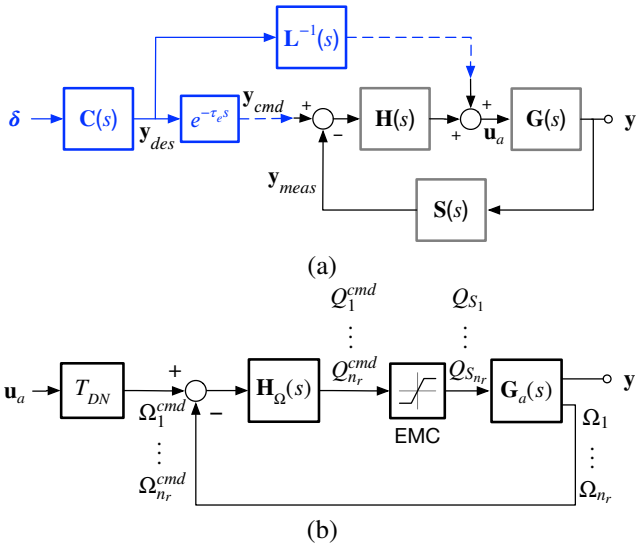

Figure 2. Model-following control system: (a) general architecture, and (b) rotor speed control loops.

ure 2) was used to enable the handling qualities assessment of conceptual designs. Figure 2a illustrates the key elements of the flight control system as implemented in Ref. 5. Additional feedback loops in Figure 2b were added for rotor speed control. This choice of architecture offered a tractable method for independent feedback stabilization and command shaping for the heave, roll, pitch and yaw axis, but is by no means the only choice.

A command model $\mathbf{C}(s)$ interprets pilot inputs $\boldsymbol{\delta}$, shaping them into a desired vehicle response $\mathbf{y}_{des}$. $\mathbf{L}(s)$ is a low-order equivalent system (LOES) approximation of the open-loop aircraft rate dynamics $\mathbf{G}(s)$, over a desired frequency range of interest (1–10 rad/s, in this instance). This feed-forward component provides lead compensation through the inversion of the LOES model, estimating input $\mathbf{u}_a$ to achieve the desired response. The role of the regulator $\mathbf{H}(s)$ is, firstly, to guarantee stability of the aircraft, and secondly, to ensure accurate tracking of the command by minimizing the error between commanded and measured output (via sensors $\mathbf{S}(s)$). The basic elements of the rotor speed control loops were: a pre-defined control allocation matrix, T_{DN}; a rotor speed error feedback compensator, $\mathbf{H}_\Omega(s)$; the engine and engine speed controller; and the bare-airframe aircraft aerodynamic model, $\mathbf{G}_a(s)$ (a reduced-order model of Eq. 3 retaining only $\boldsymbol{x}_b$ and $\boldsymbol{x}_r$). Here, rotor speed signals were fed back and compared against commanded speeds from the allocation matrix T_{DN} to determine rotor speed error signals. The rotor speed control compensator $\mathbf{H}_\Omega(s)$ specifies torque commands required to regulate rotor speeds with minimal error. The Electric Motor Controller (EMC) units are torque feedback control systems that produce the commanded engine torque output. EMC units are high-bandwidth electric components that respond at frequencies much higher than those required for flight control. Perfect response of the EMC to the commanded torque was assumed unless a physical power or torque limit of the motor was reached. Neglecting the electrical complexities of motor control, the EMCs were assumed to act as saturation elements.

Table 2. Feedback optimization constraints.

Specification	Requirement	Loop
Hard Constraints		
Eigenvalue stability	$\mathrm{Re}(\lambda) < 0$	All
Steady-state error	0.5 dB	RSC
Gain Margin	6.0 dB	All
Phase Margin	45 deg	All
Nichols Margins	Special	PFC
Response damping	0.9	RSC
Soft Constraints		
Eigendamping (0.5–4 rad/s)	0.35	All
Eigendamping (4–20 rad/s)	0.2	All
DRB	1.0 rad/s	Heave
DRB	0.9 rad/s	Roll
DRB	0.5 rad/s	Pitch
DRB	0.7 rad/s	Yaw
DRP	5.0 dB	PFC
OLOP	Special	PFC[a]
Min. crossover frequency	0.5 rad/s	Heave
Min. crossover frequency	2.5 rad/s	Roll
Min. crossover frequency	2.0 rad/s	Pitch
Min. crossover frequency	0.5 rad/s	Yaw
Min. crossover frequency	4.0 rad/s	RSC
Summed Objectives		
Max. crossover frequency	10 rad/s	All
Actuator RMS [b]	1.5	All

[a] Not applied to yaw axis
[b] Applied to engine group motors if used for RPM control

Requirements To adopt handling qualities into the conceptual design, it was necessary for the design framework to accommodate appropriate performance requirements. The CONtrol Designer's Unified InTerface (CONDUIT) software (Ref. 19) was used, for this purpose, to synthesize the feedback and command model control system gains based on requirements from Tables 2 and 3.

Feedback design requirements included stability margin and closed-loop disturbance rejection performance requirements from aeronautical standards (Refs. 20, 21) and others that encompass good general feedback design practices. Tuning of the command model gains responded to requirements for small- and large-amplitude attitude changes for attitude command-attitude hold (ACAH) response types in pitch and roll, rate command-direction hold (RCDH) in yaw, and rate command-height hold (RCHH) in yaw from the Aeronautical Design Standard-33 (ADS-33E-PRF), now MIL-DTL-32742 (Ref. 21), for military rotorcraft. Both limited and moderate agility sets of requirements were considered for the large-amplitude roll and pitch attitude change requirements. Open-Loop Onset Point (OLOP, Ref. 22) criteria were not set as constraints, but were checked to investigate the integrated effect of torque limits on the inter-connection between response type handling qualities specifications (bandwidth and agility)

Table 3. Command model optimization constraints.

Specification	Requirement	Axis
Soft Constraints		
Heave mode	0.6 rad/s	Heave
Bandwidth	2 rad/s	Roll
Bandwidth	2 rad/s	Pitch
Bandwidth	0.5 rad/s	Yaw
Heave time delay	0.2 s	Heave
Phase delay	0.9 s	All
Achievable rate	160 ft/min	Heave
Achievable attitude (limited agility)	± 15 deg	Roll
Achievable attitude (limited agility)	± 15 deg	Pitch
Achievable attitude (moderate agility)	± 60 deg	Roll
Achievable attitude (moderate agility)	−30, +20 deg	Pitch
Achievable rate	± 9.5 deg/s	Yaw
Check Only		
OLOP	Special	[a]
Attitude quickness	Special	All
Summed Objectives		
Actuator RMS[b]	1.5	All

[a] Not applied to yaw axis
[b] Applied to engine group motors if used for RPM control

and PIO susceptibility (from engine torque limit saturation).

Motor Limits

The handling qualities impact of motor torque saturation nonlinearities in the flight dynamics of eVTOL aircraft was demonstrated experimentally in Ref. 13. Torque-speed curves of the motor technology likely used with eVTOL aircraft, especially with RPM-controlled eVTOL, were needed to account for these effects during the conceptual design. A physics-based derivation of the electric propulsion components is described in the Appendix. The model was capable of producing the torque-speed curve of both Pulse Magnet Synchronous Motors (PMSMs) and Brush-Less Direct Current (BLDC) motors, and was used to calculate the torque and speed margins at a given steady-state operating point of the motor. A notional curve illustrating the definition of the torque and speed margins is shown in Figure 3.

The motor curves in Figure 3 were anchored by the peak and rated torques calculated from the sizing task at the base and rated (or specification) speeds. The curve was then projected out to the no-load condition. There is a region beyond the base motor curve where the motor can operate with specialized flux-weakening control technology, up to the no-load speed. It was also assumed that battery voltage could be slightly increased beyond the motor's rated voltage to allow torque to remain constant between the base and rated speed. The no-load speed computed at the motor's rated DC voltage marks the maximum speed limit of the motor.

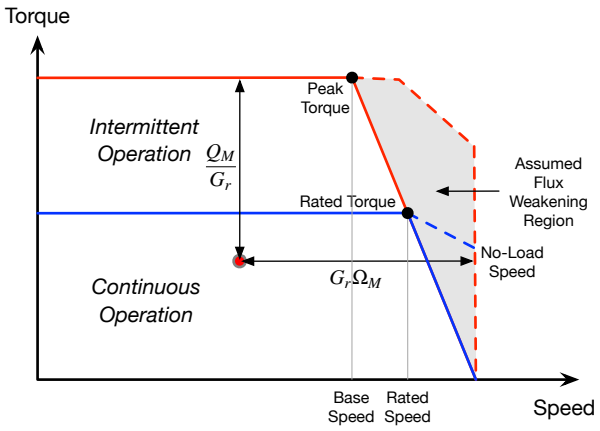

Figure 3. Notional PMSM torque-speed curve.

EXPLORATION OF THE DESIGN SPACE

Concepts

Two vehicle architectures were explored in this study: 1) a fixed rotor speed, variable blade pitch quadrotor (Figure 4a), and 2) a variable rotor speed, fixed blade pitch hexacopter (Figure 4b). Both are battery powered. The drive system for the quadrotor (Ref. 2) linked four engine groups with electric motors to a single propulsion group that provided power to all four rotors. The hexacopter distributed the propulsion over six independent groups, each with one engine group linked directly to a single rotor through a gear box. Both configurations had articulated rotor designs with matching flap frequency (1.03/rev), and baseline designs were sized to the same design disk loading (3 lb/ft^2) and blade loading coefficient (C_W/σ =0.09). A summary of the main characteristics of the two designs is shown in Table 4.

Effect of Disk and Blade Loading on Size

Disk and blade loading were varied for the hexacopter from 3–9 lb/ft^2 and 0.09–0.12, respectively. Consistent with Ref. 2, the lower design disk loading values arrived at more lightweight designs (Figure 5). By contrast, the blade loading coefficient had a much smaller but still appreciable effect (approximately 10–19% reduction for C_W/σ of 0.12 relative the baseline 0.09). This reduction was most significant at high disk loading.

It is worthwhile pointing out that aircraft principal axis radii of gyration were assumed to scale with rotor diameter during the sizing task, so effect of aircraft mass on moments of inertia is not direct.

$$I_{xx} = m(k_x R)^2 \tag{4}$$

$$I_{yy} = m(k_y R)^2 \tag{5}$$

$$I_{zz} = m(k_z R)^2 \tag{6}$$

where $k_x = 0.6$, $k_y = 0.9$ and $k_z = 1.0$ were estimated from the mass properties of the baseline design.

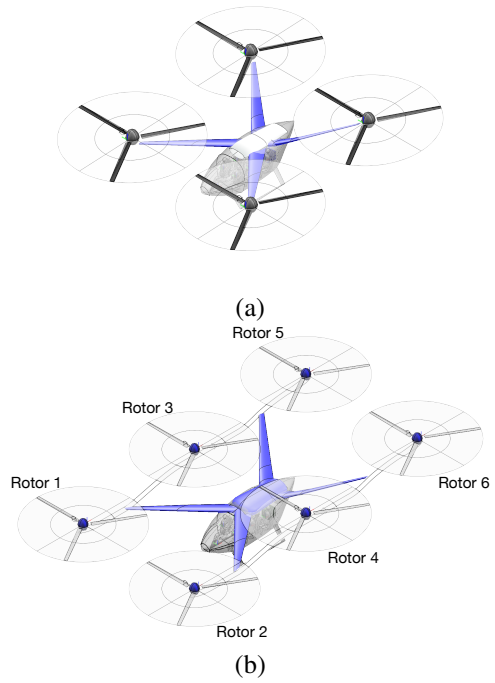

Figure 4. Renderings of the concept designs: (a) Quadrotor, and (b) Hexacopter.

Table 4. Concept design aircraft characteristics.

Characteristic	Quad	Hex
Design Gross Weight (lb)	6,427	6,510
Payload (lb)	1,200	1,200
Empty Weight (lb)	5,216	5,299
Capacity (Pax + Crew)	6	6
Number of Rotors	4	6
Design Disk Loading (lb/ft^2)	3.0	3.0
Number of Blades	3	3
Blade Pitch@75% (deg)	–	10.0
Rotor Radius (ft)	13.1	10.7
Solidity, thrust-weighted	0.056	0.056
Design Tip Speed (ft/s)	550	550
Design Rotor Speed (rad/s)	42	51.3
Design Rotor Speed (rpm)	401	490
Flapping Frequency (1/rev)	1.03	1.03
Lock Number	5.16	4.61
Propulsion Group	Central	Direct
Number of Motors	4	6
Engines		
– MCP per Motor (hp)	111.5	87.0
– MRP per Motor (hp)	167.2	130.4
– Specification Speed (rpm)	8,000	8,000
– Shaft Power Limit (hp)	319.9	211.7
Drive Torque Limit (ft · lb)	8,320	1,136
Battery Capacity (MJ)	1,316	1,449

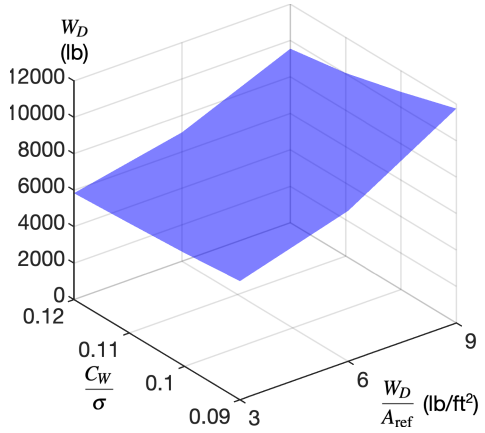

Figure 5. Hexacopter Design Gross Weight.

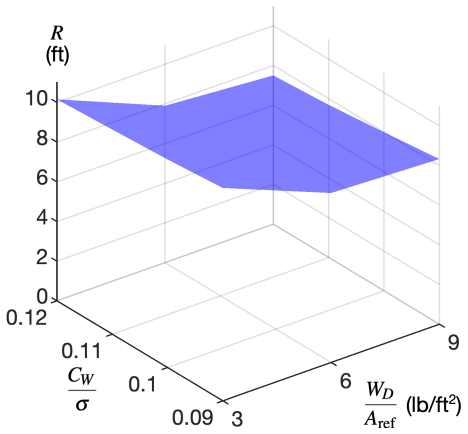

Figure 6. Hexacopter rotor radius.

Rotor diameter was not constrained during sizing, resulting in diameters spanning the 15–20 ft range over the design space (Figure 6). This approach differed from that in Ref. 2 for the Lift+Cruise, where a hard constraint on diameter of 10 ft was imposed in consideration for the possibility of the rotor inertia increasing beyond the capability of RPM control to provide enough responsiveness for maneuvering. The wisdom of this hypothesis is revised here.

Caution should be employed, for example, when assuming that a smaller radius will automatically translate to a smaller moment of inertia. Compared to the rotational moment of inertia of the turbo-electric Lift-Cruise design from Ref. 2, which was estimated at 14–27 slug · ft^2, rotor inertias for these Hexacopter designs were notably larger, ranging from 30 to over 70 slug · ft^2 (Figure 7). While rotor diameter for the Hexacopter was minimum at the highest disk loading of 9 lb/ft^2, rotor inertia was not. Finally, notable reductions in the rotor inertia were achieved for higher blade loading because of reductions in rotor solidity.

While weight, rotor size and inertia parameters can affect maneuverability in one way or another, it might be unwise to extract strong conclusions about the overall maneuverability from individual parameters because there are complex competing interdependencies at play. Referring back to the design

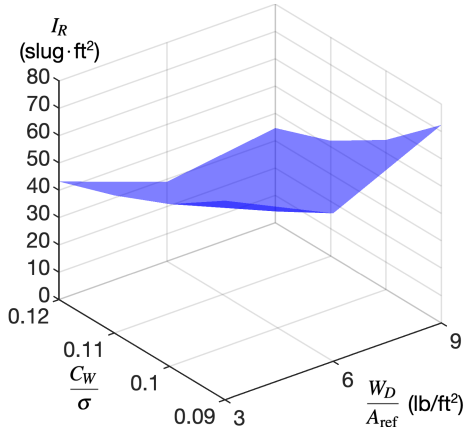

Figure 7. Hexacopter rotor moment of inertia.

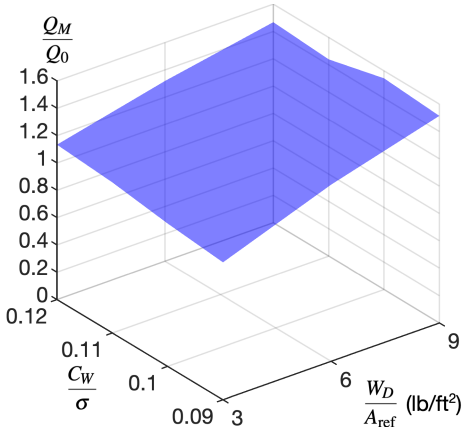

Figure 8. Hexacopter mean relative torque margin.

assumptions for the Lift-Cruise from Ref. 2, for instance, it does take larger torques to impart the same acceleration on a rotor with larger rotational inertia, and presumably, radius. The effectiveness of rotors for RPM control increases with size (Ref. 12), however, because

$$\frac{\partial T}{\partial \Omega} \approx \frac{2T}{V_{tip}} R \tag{7}$$

For a constant thrust (set by aircraft design gross weight) and design tip speed (usually set by acoustics or performance requirements), Eq. 7 implies that smaller rotors need to be accelerated to higher speeds to get same thrust response.

With smaller rotors and more weight, the capability of RPM control to provide enough responsiveness for maneuvering would seem to be put into question for higher disk loading. However, additional characteristics or parameters need to be considered. For instance, because of the scaling of Eqs. 4–6, perhaps a drawback of the approach, the differences in the moments of inertia tended to be small. The achievable maneuverability also depends on the motor torque margins available for maneuvering (Figure 8), as well as the aircraft stability characteristics. A formal analysis of the vehicle dynamics that weighs all of these factors together follows in the next few sections.

Effect of Disk and Blade Loading on Maneuverability

Maneuverability of an aircraft is the quality it has of being easy to move or direct while in motion. There are three fundamental characteristics of a dynamic system that govern its maneuverability: 1) its stability, 2) the effectiveness of the control mechanisms, and 3) the maximum control input that can be applied. It is an interesting aspect of dynamic systems that the more stable they are, the harder they are to maneuver. High maneuverability therefore requires low stability. Effectiveness of the controls measures how much rate of change can be generated per unit of control input. And of course, how large of a control input can be applied to the system will determine the overall maximum rate of change that can be imparted on it.

The simplest dynamic system that captures these key factors is a first-order ordinary differential equation such as Eq. 8:

$$\dot{x}(t) = ax(t) + bu(t) \tag{8}$$

or

$$X(s) = \frac{b}{s-a} U(s) \tag{9}$$

in the Laplace domain. Here stability is measured by the a coefficient, and the control effectiveness is determined by the control derivative b. It is helpful to normalize the control derivative from Eq. 8 such that the control input limits are ± 1.

If so, then the maximum theoretical steady state response is given by the unit step input response of this system. From the final value theorem applied to Eq. 9 this is:

$$\lim_{t\to\infty} x(t) = \lim_{s\to 0} sX(s)\frac{1}{s} = -\frac{b}{a} \tag{10}$$

Applying these ideas to the Hexacopter model, to first-order approximation, the linear heave, roll, pitch and yaw dynamics can be simplified to

$$\dot{w} = Z_w w + \sum_{i=1}^{n_r} Z_{Q_i} c_{i,\text{col}} \cdot \hat{Q}_{\text{col}} \tag{11}$$

$$\dot{p} = L_p p + \sum_{i=1}^{n_r} L_{Q_i} c_{i,\text{lat}} \cdot \hat{Q}_{\text{lat}} \tag{12}$$

$$\dot{q} = M_q q + \sum_{i=1}^{n_r} M_{Q_i} c_{i,\text{lon}} \cdot \hat{Q}_{\text{lon}} \tag{13}$$

$$\dot{r} = N_r r + \sum_{i=1}^{n_r} N_{Q_i} c_{i,\text{dir}} \cdot \hat{Q}_{\text{dir}} \tag{14}$$

where $\hat{Q}_{\text{col}}$, $\hat{Q}_{\text{lat}}$, $\hat{Q}_{\text{lon}}$ and $\hat{Q}_{\text{dir}}$ represent axis-aligned shaft torque control inputs, and $c_{i,\text{input}}$ are the control input allocation coefficients to the i-th rotor shaft. Stability and control derivatives are obtained from a 6-dof reduced-order equivalent model of Eq. 3. This simplification clearly neglects the rotor speed dynamics, but is appropriate for the theoretical estimation of the steady state responses in Figures 9–12, calculated as per Eq. 10.

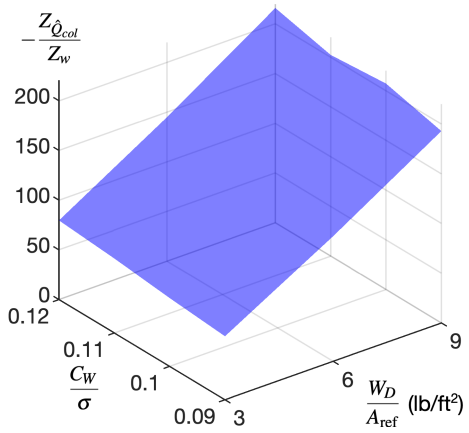

Figure 9. Maximum steady state heave response.

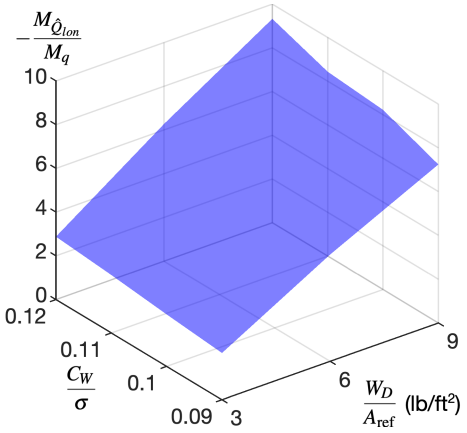

Figure 11. Maximum steady state pitch rate response.

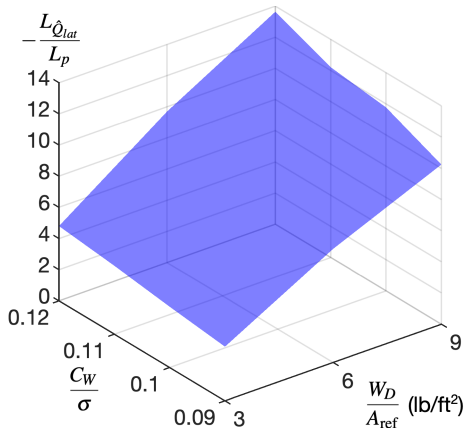

Figure 10. Maximum steady state roll rate response.

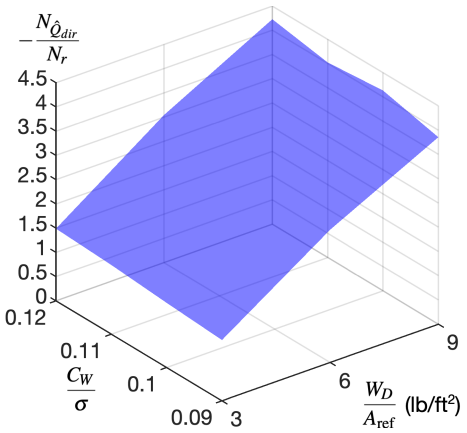

Figure 12. Maximum steady state yaw rate response.

Control allocation coefficients $c_{i,\text{input}}$ were defined such that maximum torque was applied to each individual rotor for a unit step input of the designated axis-aligned torque input $\hat{Q}_{\text{input}}$. With increased design gross weight, aircraft engines, which tended to be sized by the 900 ft/min rate of climb requirement, were larger for the higher disk loading and offered additional margins for maneuverability at the hover off-design flight condition. Results suggested a significant improvement in maneuverability is likely for higher disk and blade loading. This was attributable to various factors, but mainly to: 1) lower damping coefficients Z_w, L_p, M_q and N_r, but most importantly, 2) larger powertrain torque margins.

Motor Sizing

A key limitation not properly addressed in the preliminary sizing results shown above was the motor operating speed. Inspection of the vehicle state for each sizing flight condition and mission segment, revealed that the no-load speed of the motor was exceeded under certain conditions. Most critically, the 900 ft/min climb to cruise altitude mission segment drove the motors for the two rear rotors to operate over $10,000$ rpm. Results presented in this section illustrate the motor torque-speed curve sizing process, and how motor operation differs for multirotor designs with fixed-pitch, variable-speed rotors versus variable-pitch, fixed-speed rotors. A Hexacopter design is first resized to ensure motor operating speed is within the limits of the motor, and to build in additional torque margins for maneuvering control. The resulting motor curves are then presented. Motor curves for the quadrotor design are then shown for comparison.

Resized hexacopter The baseline hexacopter configuration, with $W_D/A_{\text{ref}} = 3$ lb/ft^2 and $C_W/\sigma = 0.09$, was selected for redesign. Arguably, one of the first design parameters to be varied should be the blade loading coefficient, as this could confer slight improvements in maneuverability and reductions in design gross weight. The design disk and blade loading were kept constant, regardless. This configuration was still lightweight, which made it attractive from a design (and associated cost) perspective. It was in fact the potential maneuverability deficiencies of this design that made it an interesting case study to exercise the broader capabilities of the toolset, including a more detailed handling qualities analysis. From a technical point-of-view it was of interest to: 1) assess handling qualities of the design, and 2) investigate whether handling qualities could be improved through redesign of key parameters.

Table 5. Resized Hexacopter design characteristics.

Characteristic	Baseline	Redesign
Design Gross Weight (lb)	6,510	6,758
Payload (lb)	1,200	1,200
Empty Weight (lb)	5,299	5,548
Max. Take-Off Weight (lb)	8,557	9,404
Number of Rotors	6	6
Design Disk Loading (lb/ft^2)	3.0	3.0
Design Blade Loading (C_W/σ)	0.09	0.09
Number of Blades	3	3
Blade Pitch@75% (deg)	10.0	12.5
Rotor Radius (ft)	10.7	10.9
Solidity, thrust-weighted	0.056	0.056
Design Tip Speed (ft/s)	550	550
Design Rotor Speed (rad/s)	51.3	50.3
Design Rotor Speed (rpm)	490	480
Flapping Frequency (1/rev)	1.03	1.03
Lock Number	4.61	4.67
Engines		
– MCP per Motor (hp)	87.0	118.3
– MRP per Motor (hp)	130.4	177.5
– Specification Speed (rpm)	8,000	8,000
– Shaft Power Limit (hp)	211.7	244.7
– Transmission Gear Ratio	16.3	15.0
Drive Torque Limit (ft · lb)	1,136	1,337
Battery Capacity (MJ)	1,449	1,461

As seen in Table 5, the differences in size between the baseline and redesigned hexacopter model were minimal. Again, the first aspect to address was the motor speed, which was found to exceed the no-load speed of the motor when contrasted against the associated motor torque-speed curves. Increasing the rotor blade pitch was found to alleviate this slightly, enabling rotors to trim to lower speeds. Adjusting the gear box ratio between the engine groups and rotors presented another means of reducing the motor speed, while maintaining the rotor speeds relatively constant over the sizing conditions. Both of these design variations helped ensure feasible operating speeds for the motor, but neither provided better torque margins.

The clearest way to improve the torque margin during the NDARC sizing task was to reduce the fraction of power available f_P from Eq. 1. Fraction f_P for the sizing mission segments was reduced to 0.75 from the baseline 0.95 value. Subsequent results in this section are solely for this resized design.

The hexacopter's six motors were identical. Motor coefficients, as derived by the sizing methodology described in the Appendix, are depicted in Table 6. It was observed that the motor's base speed of 7,228 rpm and rated speed of 7,988 rpm were close in value, but not exactly equal to, NDARC's prescribed base and specification speeds (7,200 and 8,000 rpm, respectively). Differences in the motor speeds were explained by the convergence criteria chosen to solve for the flux linkage in Eq. A-18. The motor speed difference could be reduced by tightening up convergence criteria and reducing step size of power factor iteration, but the difference was found to be negligible. The motor power factor was 0.942. The motor power factor depends very much on the distance between the rated speed and base speed, as well as on the ratio of MRP to MCP. Increasing the distance between the base speed and rated speed would likely result in a lower power factor, which may increase the no-load speed.

Table 6. Resized Hexacopter motor specifications

Motor Specifications	Redesign
Maximum Rated Power (hp)	177.4
Peak Power @ 8,000 rpm (hp)	196.3
Peak Torque (ft · lb)	128.9
Base Speed (rpm)	7,228
Maximum Continuous Power (hp)	118.1
Maximum Continuous Torque (ft · lb)	76.6
No-load speed (rpm)	8,621
Rated Speed (rpm)	7,988
Power Factor	0.942
Number of pole pairs	6
Flux Linkage (Wb)	0.0692
Back-EMF Constant (Vs/rad)	0.4154
Stator Resistance (Ω)	0.0393
Q-axis Self-Inductance (mH)	0.1448
D-axis Self-Inductance (mH)	0.1448
Rated Motor Voltage (V)	650

Table 7. Hexacopter rotor torque margins (ft · lb)

No.	Flight Condition	R1&2	R3&4	R5&6
1	Hover MTOW, 6k/ISA	593	651	707
2	V_{br}, 500 ft/min ROC, 10k/ISA	1,124	995	866
4	Miss. Segments 2 & 11	952	994	1,036
5	Miss. Segments 3 & 12	967	1009	1,050
6	Miss. Segments 4 & 13	948	827	662
7	Miss. Segments 5 & 14	1,358	1,218	1,079
8	Miss. Segments 6 & 15	967	1,009	1,050
9	Miss. Segments 7 & 16	967	1,009	1,050
10	Miss. Segments 8 & 17	981	1,023	1,064
21	Miss. Segment 19	1,480	1,371	1,267
22	V_{br}, 6k/ISA	1,355	1,217	1,082
23	V_{be}, 6k/ISA	1,479	1,370	1,267
24	V_{max}, 6k/ISA	1,145	1,014	870
25	Hover, SL/ISA	968	1,010	1,052
26	Hover, 6k/ISA	967	1,009	1,050
27	Hover, 10k/ISA	966	1,008	1,049

The torque and speed margins of rotors determine the range that is left over for dynamic maneuvering after trimming the aircraft. Rotor torque margins from sizing, mission and off-design conditions are presented in Table 7. Mission segments 1 and 8 were omitted as both corresponded to an idle condition with low torque and speed requirements. Condition 1, at maximum takeoff weight (MTOW), possessed the lowest torque margin on the 1st and 2nd rotors (R1 and R2 in Table 7), reported as 593 ft · lb. Note that MTOW here was calculated for

$f_P = 0.8$. If computed at 100% of installed power there would have been no margins for control available. Mission segments 4 and 13 (900 ft/min climb conditions) had the lowest torque margin on the 5th and 6th rotors (662 ft · lb). Most rotor torque margins were near 1,000 ft · lb.

Rotor speed margins are presented in Table 8. The 900 ft/min climb condition of segments 4 and 13 (condition 6) was also observed to have the lowest speed margin of 31 rpm, for rotors 5 and 6. This speed margin could potentially be improved, with a further reduction in gear ratio. Further reductions in gear ratio could mean an increase in torque and motor weight, however. Rotors 1 and 2 from condition 1 had a speed margin of 68 rpm. Rotors 5 and 6 from condition 2 had a speed margin of 51 rpm.

Table 8. Hexacopter rotor speed margins (rpm)

No.	Flight Condition	R1&2	R3&4	R5&6
1	Hover MTOW, 6k/ISA	68	79	91
2	V_{br}, 500 ft/min ROC, 10k/ISA	104	78	51
4	Miss. Segments 2 & 11	143	152	162
5	Miss. Segments 3 & 12	145	155	164
6	Miss. Segments 4 & 13	81	56	31
7	Miss. Segments 5 & 14	146	120	94
8	Miss. Segments 6 & 15	145	155	164
9	Miss. Segments 7 & 16	145	155	164
10	Miss. Segments 8 & 17	148	157	167
21	Miss. Segment 19	209	193	177
22	V_{br}, 6k/ISA	170	146	123
23	V_{be}, 6k/ISA	209	193	178
24	V_{max}, 6k/ISA	127	99	71
25	Hover, SL/ISA	182	191	200
26	Hover, 6k/ISA	145	155	165
27	Hover, 10k/ISA	118	128	138

The location of operating points with respect to maximum continuous torque (MCT) which was at 76.6 ft · lb is crucial. Motors for most design and off-design flight conditions were under MCT as observed by tight groupings of the torque-speed-efficiency motor map produced within Figure 13. The 5th and 6th motors from condition 6 operated above MCT by 4.2 ft · lb, in the region of flux-weakening. The 5th and 6th motors from condition 6 also exceeded the rated speed by 168 rpm. All motors from condition 1, at MTOW, operated above MCT.

It was observed that almost all motors operated above 95.5% efficiency; 95% motor efficiency was a target efficiency to match the prescribed model in NDARC. The efficiency map in Figure 13 did not include losses from 3-phase inverter efficiency, which is why 96% efficiency was originally targeted during coefficient sizing instead of 95% efficiency assumed in NDARC. The computed motor map efficiencies include winding and permanent magnet temperature variations, away from the intersection of No-Flux Weakening (NFW) and MCT in Figure 13.

When operating points cross NFW, the motor depends on a combination of higher battery voltage than the rated motor voltage and flux-weakening control laws to operate effectively. The Flux-Weakening (FW) line depicted in Figure 13 shows the predicted extensions of peak torque and MCT with speed. For typical motors operating at the rated motor voltage, torque starts to gradually roll off near the base speed, and power may or may not be constant immediately after the base speed depending on the flux-weakening algorithm employed.

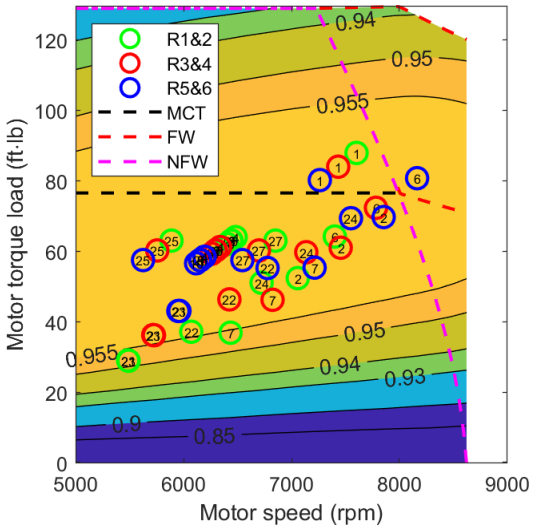

Figure 13. Hexacopter torque, speed and efficiency map.

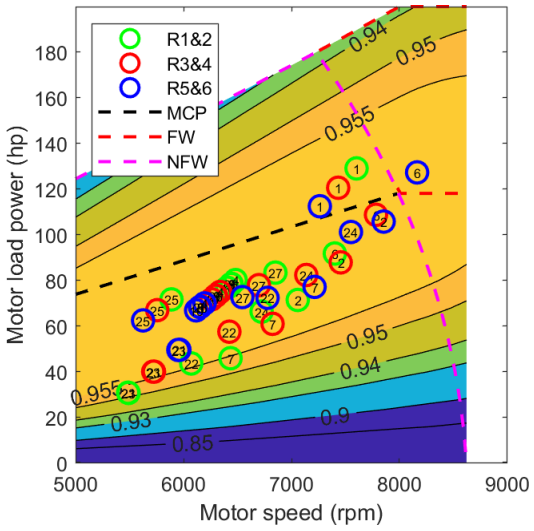

Figure 14. Hexacopter power, speed and efficiency map.

The hexacopter design and off-design motor operating points were placed on a speed-power-efficiency map as in Figure 14. Here the power was allowed to increase after the base speed through a combination of flux-weakening control and higher battery voltage than the motor rated voltage of 650 V, up until the rated speed of 7,988 rpm, where it was held constant. Motor manufacturers do provide a range of voltage for their

motors which exceeds the rated motor voltage often by several hundred volts.

A key point of Figure 14 is that power available could be made to exceed the MRP depending on specific architectural design choices of the electric powertrain. Notably, NDARC was not allowed to utilize this additional power during sizing, but flux-weakening control could conceivably be used to increase powertrain margins for maneuvering. Thermal implications of continuous operation in this region will be discussed next.

The 5th and 6th motor exceeded the rated speed and MCT during the 900 ft/min climb to cruise altitude (condition 5); this called into question if operations in an intermittent region of the motor map, the motor winding temperature might exceed 140 °C. The entire NDARC design mission was simulated to check the winding temperature of each motor over the mission. Conditions 1 and 2 were not technically part of the successive design mission points, so they were excluded in the analysis. So were the reserve mission segment 19 (condition 21) and off-design analysis conditions (conditions 22–27).

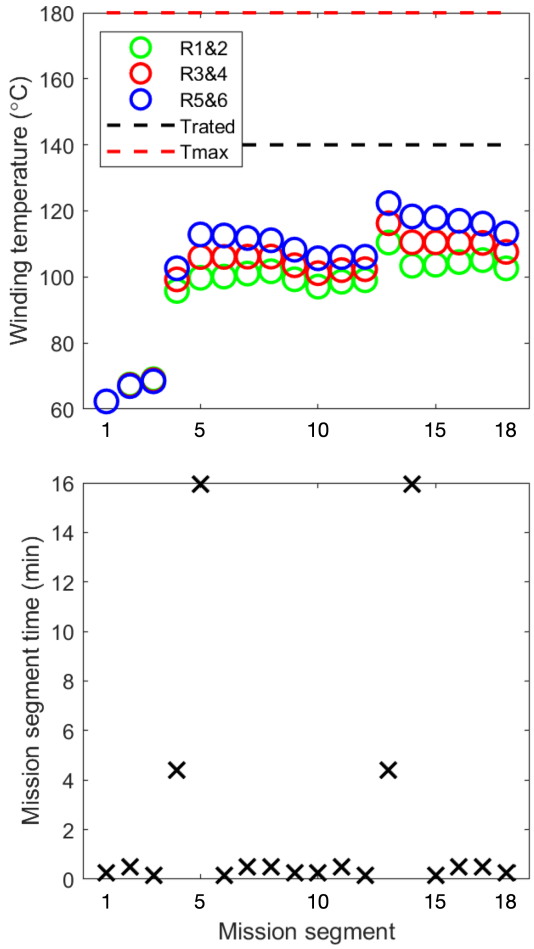

Figure 15. Top) Hexacopter motor winding temperature; bottom) individual mission segment time.

The temperature simulation results shown in Figure 15) initially assumed that the motors were at idle for 300 minutes, giving temperature time to converge. A rise in temperature was observed in all motor windings for mission segment 4, corresponding to the approximately 4.5 minute climb at 900 ft/min. The temperatures gradually reduced over the rest of the mission, until segment 13 when another 4.5 minute climb at 900 ft/min was initiated. It was observed that for the design mission points, the winding temperature of the 5th and 6th motors, never exceeded the rated temperature. There are two main reasons for this. The first reason was that prior and following design mission segments end at significantly lower winding temperatures than the rated temperature. The second reason was that the time constant of the motor temperature model was approximately 10 minutes.

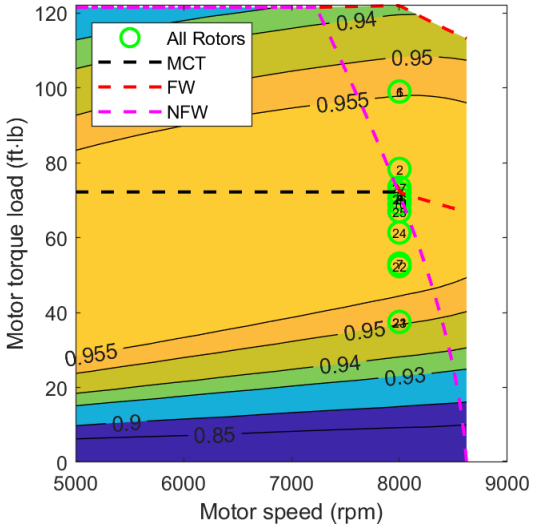

Figure 16. Quadrotor torque, speed and efficiency map.

Quadrotor For comparison, a collective blade-pitch controlled quadrotor torque-speed-efficiency motor map was also generated (Figure 16). It was observed that the motors were placed at the specification speed and appear in a vertical line for all flight conditions. The most critical conditions were 1 and 6 which overlap almost on top of each other in Figure 16. These same conditions were also observed to be crucial for the hexacopter. For the blade-pitch controlled vehicles, where the engine group does not double as primary flight control actuator, speed and torque margins are less critical. Specific tabulated margins are therefore not shown. However, it was observed that, like the hexacopter, quadrotor motor torque requirements occur above MCT of 73 ft · lb, by 26 ft · lb. Therefore a temperature analysis was required on the design mission points.

The temperature analysis presented in Figure 17 indicated that operating condition did not adversely affect the motor winding temperature of the quadrotor during the design mission. Driven by the design mission, the temperatures remained below the rated condition of 140°C for the same reasons as the hexacopter. However, the winding temperature after climb segments at 900 ft/min, corresponding to conditions 6 and 15, were higher in the case of the quadrotor, than it was for

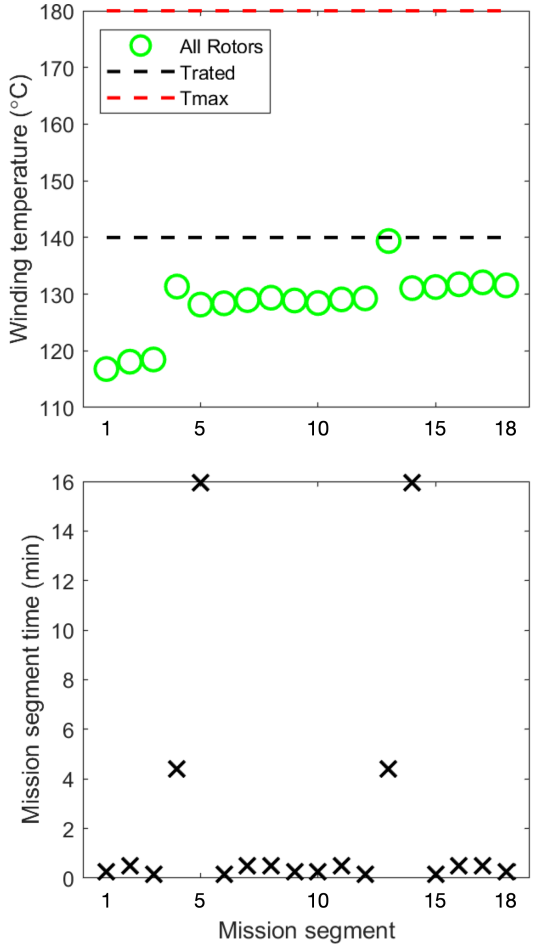

Figure 17. Top) Quadrotor motor winding temperature; bottom) individual mission segment time.

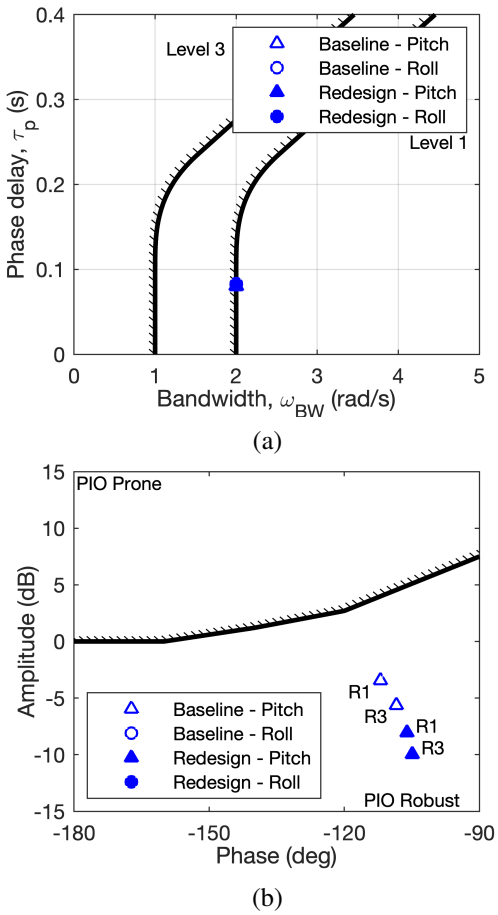

Figure 18. Baseline limited agility ACAH case: (a) small-amplitude response criteria, and (b) OLOP criteria.

the hexacopter (see Figure 15). This result could indicate that temperature is an important factor in sizing. If the design mission were to be extended and include another climb segmentt, the temperature progression in Figure 17 would suggest that the winding temperature may climb above the rated temperature, leading to reduced reliability of the powertrain.

Handling Qualities

Figures 18–20 compare the small-amplitude attitude response (bandwidth and phase delay) and OLOP (phase and amplitude) margin characteristics for the baseline and redesigned hexacopter models (both designed to $W_D/A_{\text{ref}} = 3$ lb/ft^2 and $C_W/\sigma = 0.09$). Bandwidth and phase delay characterize the short-term response for small attitude changes (pitch and roll in this case). These aircraft response qualities govern the precision with which a pilot can make small attitude corrections. The OLOP criteria quantify the likelihood of the coupled pilot-vehicle system becoming unstable if an actuator rate limit were to be activated. The OLOP criteria measure the actuator broken-loop frequency-response phase and amplitude at the so-called onset frequency, i.e., the frequency at which the actuator rate limit is activated with all feedback loops closed. Although not directly evident from the Figures 18–20, results also showed the handling qualities effects of large-amplitude attitude change requirements on these two designs. Figures 18 and 20 compare the handling qualities for a flight control system tuned to enable limited agility maneuverability as defined by achievable roll and pitch changes of $\pm$15 deg. Figure 19 shows results for a control system tuned to provide moderate agility maneuvering ($\pm$60 deg in roll and $\pm$30 deg in pitch).

Across Figures 18a, 19a and 20a it is seen how through the control synthesis it was possible to instill identical (small- and large-amplitude response) handling qualities. Although these two configurations had very similar bare-airframe dynamics, this would still hold true for aircraft with differing dynamics characteristics. The differences in handling qualities showed up in Figures 18b, 19b and 20b when assessing the impact of the motor torque limit on the OLOP criteria. The redesigned hexacopter exhibited additional protection against PIO across all three control system sets due to the extra installed torque margins. It can be seen from Figure 18 that when asked for limited agility both aircraft designs were fairly robust to PIO. In contrast, command model gain sets delivering moderate agility were found to be significantly more PIO prone (Figure 19). Similarly, Figure 20 showed there were limits to how

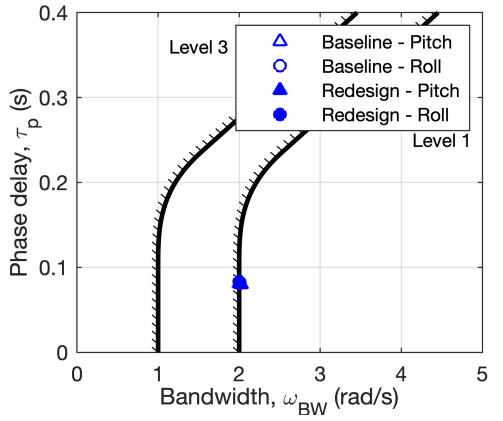

(a)

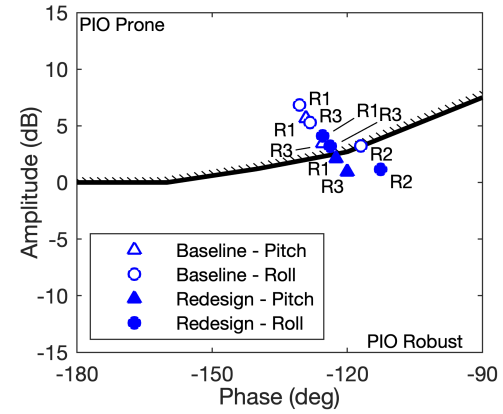

(b)

Figure 19. Low-bandwidth moderate agility ACAH case: (a) small-amplitude response criteria, and (b) OLOP criteria.

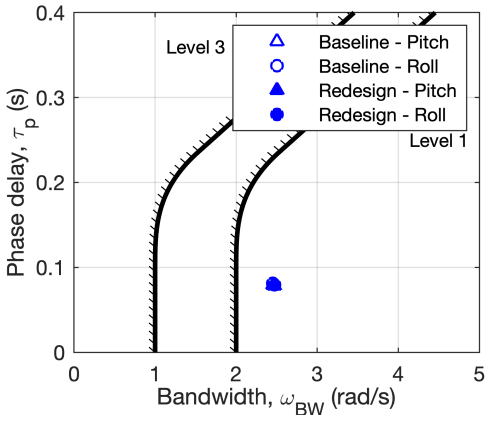

(a)

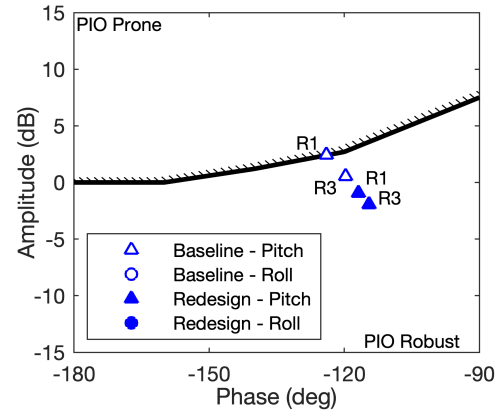

(b)

Figure 20. High-bandwidth limited agility ACAH case: (a) small-amplitude response criteria, and (b) OLOP criteria.

much bandwidth could be extracted from these two designs.

Despite longer moment arms, only four of the rotors were active for pitch control. This, coupled with a doubling of the pitch moment of inertia, would explain why pitch control tended to be more prone to PIO: motors needed to work about 65% harder in pitch than in roll. Roll control only exhibited a propensity for PIO with the moderate agility flight control laws, but it is pointed out that large-amplitude roll attitude change requirements were twice as high. Incidentally, this result was consistent with Figures 10 and 11.

DISCUSSION

Four separate tools were exercised throughout this study to conduct a conceptual design exploration of eVTOL aircraft handling qualities. Of primary concern was the investigation of the handling qualities of RPM-controlled eVTOL multirotor aircraft. The tools utilized were: 1) NDARC for the aircraft sizing and performance analysis, including the calculation of trim; 2) FlightCODE, a flight dynamics modeling and analysis tool capable of rapid generation of linear stability and control derivative models and control analysis; 3) CONDUIT aided in the handling qualities-centric control law optimization; and 4) an electric motor physics-based sizing tool used to model the torque-speed characteristic curves and the efficiency map of the motor from the available power and peak torque.

The various tools are not currently tightly integrated, so a certain amount of manual iteration was needed. For instance, left unconstrained, NDARC produced motor speeds during the sizing task that invalidated the no-load speed predicted by the physics based motor models. The motor sizing tool was used here as a means of verifying the feasibility of the design after sizing was completed. Future work should investigate how to streamline the toolchain "data flow" and interaction.

Sizing of an RPM-controlled Hexacopter concept explored the dependency of aircraft size to the fundamental design parameters: 1) disk loading and 2) blade loading coefficient. Design tip speed was kept constant at 550 ft/s. The design gross weight was observed to almost double for a disk loading of 9 lb/ft^2 compared to the baseline 3 lb/ft^2 value. Rotor diameter decreased by about 20%, commensurate with the weight and disk loading changes.

Perhaps the more interesting results from this parametric investigation lay in the assessment of the flight dynamics: a first-order approximation of the stability and control parameters revealed that the heavier aircraft designs, sized to the higher disk loading and blade loading coefficients values,

were potentially and significantly more agile. Overall, agility increased approximately three-fold compared to the baseline disk and blade loading design. This large difference in agility was attributed to a number of factors including a reduction in the damping coefficient, a slight increase in the control effectiveness, but also notable growth in the engine size conferring these designs with higher control authority.

The final discussion point pertains to the different approaches taken for the conceptual design assessment of flight dynamics. The flight dynamics modeling tool enabled a very rapid assessment of design maneuverability based purely on the linear perturbation model of Eq. 3. For context, given the aircraft description and trim information from NDARC, the generation of the data for Figures 5–12 was executed in a matter of minutes (less than a minute per case for an ordinary 2.4 GHz consumer grade processor). This approach weighed the three fundamental flight dynamics governing parameters: 1) stability (linear stability damping coefficient), 2) control effectiveness (linear control derivative), and 3) control margins (the physical motion, rate or load limits of the actuator, e.g., the torque limit of the engine for RPM control). It, however, neglected transient, actuator or relevant modal dynamics. This is not to say that further analysis of the models from Eq. 3 could not deliver this type of information, simply that it was not presented here.

Further analysis was needed to generate actionable handling qualities information. CONDUIT was used to synthesize an optimal set of flight control laws, given an assumed control system architecture. When recast into this form the problem allowed for the trade-off analysis of concrete handling qualities specifications, e.g., pilot input response type characteristics, while assessing whether the design had sufficient control authority. This CONDUIT-enabled approach presented a powerful capability, but was dramatically more computationally intensive. Only one of the designs was therefore picked to undergo a more detailed handling qualities trade-off study. There was no intent to produce an optimally redesigned aircraft, but only to demonstrate tool utilization. Reducing the fraction of power available for the sizing task produced slightly heavier RPM-controlled hexacopter designs with larger engines, higher control authority, and ultimately more robustness to PIO (and hence, improved handling qualities).

In a sense, this approach was representative of the problems likely faced by fly-by-wire flight control system designs: advanced flight control modes that simplify the task of the pilot and reduce workload can indeed confer Level 1 handling qualities, but differences in the bare-airframe dynamics may require varying levels of authority from the control actuators. Failure of the designer to ensure adequate actuator authority can lead the aircraft exposed to potentially catastrophic handling qualities cliffs, i.e., aircraft states that when entered will result in severe and sudden degradation of the handling qualities. Crucially, the methods proposed here were demonstrated to enable the conceptual design sizing of actuators to minimize these handling qualities deficiencies.

CONCLUSIONS

The following conclusions were established on the basis of the results and discussion presented in this paper:

- A framework that automated the generation of linear perturbation state space models from the size and performance characteristics of the aircraft designs provided sufficient stability, control effectiveness and control margin to conduct a rapid assessment of the flight dynamics suitable for conceptual design.
- Agility of the hexacopter designs improved significantly when increasing the design disk loading and design blade loading coefficient to 9 $\mathrm{lb}/\mathrm{ft}^2$ and 0.12 (from 3 $\mathrm{lb}/\mathrm{ft}^2$ and 0.09), respectively.
- Increasing the disk loading up to 9 from 3 $\mathrm{lb}/\mathrm{ft}^2$ also caused significant growth in the design gross weight, from about $6,500$ to nearly $12,000$ lb.
- Post-sizing, designs frequently exceeded electric motor and thermal model speed and torque limits, suggesting that motor model limits should be integrated into the sizing task.
- A handling qualities trade-off analysis, capable of delivering actionable concrete handling qualities information, required casting the linear perturbation models and sizing information into a control synthesis and optimization framework.
- For the Hexacopter, reducing the fraction of power available to 75% during the sizing task conferred improved control authority over the baseline design, with only a modest increase in aircraft gross weight (250 lb).

Author contact: Carlos Malpica, carlos.a.malpica@nasa.gov; Peter Suh, peter.m.suh@nasa.gov; Christopher Silva, christopher.silva@nasa.gov.

APPENDIX

Motor Map Design

This section includes two subsections which cover the motor map design methodology. The motor map was considered an intuitive way of depicting available torque, power and speed of the motor, which together with design points from NDARC was used to determine torque and speed limits useable by FlightCODE. The first subsection covers motor coefficient sizing which was the process used to convert NDARC motor specifications into physics-based motor coefficients. The second subsection covers the prediction of peak torque and speed values, which in turn were used to determine rotor speed and torque limits.

Motor coefficient sizing Sized NDARC vehicles report motor specification speed (set as input), MRP, MCP, peak torque, and a power limit defined from peak torque at the specification speed. This Appendix addresses how to convert these parameters into a feasible motor map which would likely be provided by a motor manufacturer. The first step is to use NDARC motor specifications to derive motor coefficients by way of motor physics equations. Some decisions had to be made along the way for various constants used in the motor physics equations, and although not called out directly, values chosen were typically reflected in relevant motor data sheets.

The Direct-Quadrature (D-Q) frame is traditionally used to analyze operations of both Pulse Magnet Synchronous Motors (PMSMs) and brushless direct current (BLDC) motors. For direct current (DC) analysis of alternating current (AC) motors, rotations are performed successively from the three-phase frame to the alpha-beta frame to the D-Q frame fixed to the motor rotor. The steady-state vectorial schema of a circuit equivalent plotted on the D-Q axis from Ref. 23 is depicted in Figure 21.

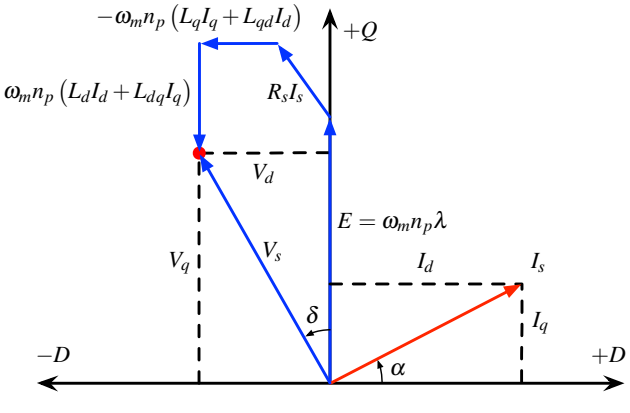

Figure 21. Steady-state phasor diagram of the PMSM.

Several assumptions were made for motor coefficient sizing. It was assumed at steady state that change in current is zero, cross-inductance terms were negligible and D-axis current was zero. The last of these three assumptions was made together with a decision to identify the NDARC motor specification speed as the motor's rated speed. The NDARC reported MRP, was determined to be the peak power of the motor. The motor's rated speed was defined as the highest speed on the torque map before flux-weakening control laws were required (i.e., D-axis current is non-zero) coinciding with the MCT operation of the motor. For simplicity, the motor type was assumed to be non-salient meaning equivalence in D-axis and Q-axis self-inductance; although in the paper, the self-inductance terms were presented as separate quantities. With these assumptions in place, the steady state Q-axis stator voltage was approximated as the summation of voltage due to torque and back-EMF as in Eq. A-1.

$$V_q \cong R_s I_q + \lambda n_p \omega_m \tag{A-1}$$

Here R_s is stator resistance, I_q is motor stator current, λ is motor flux linkage, n_p is number of pole pairs, and ω_m is rotational mechanical speed of the motor. The back-EMF constant was computed by λn_p. Motor speed ω_m was assumed to operate at a multiple of the gear ratio of the gear box connected to the aerodynamic rotor of the rotorcraft.

The D-axis stator voltage for steady state operations was computed as in Eq. A-2

$$V_d \cong -I_q L_q n_p \omega_m \tag{A-2}$$

Where L_q is the rotor Q-axis self-inductance. The motor stator voltage in Figure 21 was computed as in Eq. A-3.

$$V_s = \sqrt{V_q^2 + V_d^2} \tag{A-3}$$

AC motors are voltage limited by the DC-link voltage on the inverter. The voltage limitation was conveniently captured by the following constraint (Ref. 24) as provided in Eq. A-4

$$M = \frac{V_s}{G_{inv} V_b} \leq 1 \tag{A-4}$$

where V_b is the DC-voltage measured at the inverter terminal and G_{inv} is the inverter voltage output gain. During motor operations, the modulation ratio, M, when equal to 1 suggests inverter saturation, resulting in open loop behavior and limiting torque. The voltage constraint of the motor described by Eq. A-4 was affected by the type of inverter and gate switching logic. Gate switching logic such as sinusoidal pulse width modulation (SPWM) or space vector pulse width modulation (SVPWM) affects G_{inv} to be equal to $\frac{1}{2}$. In the context of Eq. A-4, an SVPWM inverter was assumed and G_{inv} was determined through simulation to be $\frac{1}{\sqrt{3}}$.

The design of the motor coefficients took place at the rated motor torque and speed, the condition defined as immediately before requiring flux-weakening control and the intersection of MCT. NDARC would associate the rated design point with MCP. A superscript r is appended to variables to indicate a parameter evaluated at a motor rated condition.

The motor power factor was computed from angles depicted in Figure 21 as in Eq. A-5

$$\Phi = \cos(\varphi) = \cos\left(\frac{\pi}{2} + \delta - \alpha\right) \tag{A-5}$$

where the voltage angle is solved for as in Eq. A-6

$$\delta = -\tan^{-1}\left(\frac{V_d}{V_q}\right) \tag{A-6}$$

and the current angle was solved for as in Eq. A-7.

$$\alpha = \tan^{-1}\left(\frac{I_q}{I_d}\right) \tag{A-7}$$

The current angle, α, at the rated condition of the motor is equal to $\frac{\pi}{2}$, due to the assumption that $I_d = 0$. Therefore at the

rated condition the motor power factor can be computed as in Eq. A-8.

$$\Phi = \cos(\varphi) = \cos\left(-\tan^{-1}\frac{V_d}{V_q}\right) \tag{A-8}$$

By substituting Eqs. A-1 and A-2 into Eq. A-8, the motor rated inductance can be solved for as in Eq. A-9.

$$L_d^r = L_q^r = \frac{\tan(\cos^{-1}(\Phi))\lambda^r}{I_q^r} \tag{A-9}$$

The three unknown terms in Eq. A-9 are the rated current, power factor and flux linkage. The rated current was determined as in Eq. A-10

$$I_q^r = \frac{2}{3}\frac{\tau_I}{\lambda^r n_p} = \frac{2}{3}\frac{\tau_L^r + \tau_l^r}{\lambda^r n_p} \tag{A-10}$$

where τ_I is the sum of torque loss and load torque, τ_l^r is the torque loss experienced at the rated motor condition and τ_L^r is the rated load torque. The friction model was assumed to be as in Eq. A-11

$$\tau_l^r \cong \tau_h + c_\mu \omega_m^r \tag{A-11}$$

where τ_h is hysteresis friction loss and c_μ is the viscous damping coefficient. Hysteresis torque loss was modeled to assist in sizing a hysteresis coefficient for the motor temperature model. For simplicity, the damping coefficient was calculated by assuming a percentage of torque loss with respect to the rated motor load torque. It was assumed that torque losses would amount to 2% of the rated load torque at the rated operating condition. It was assumed that hysteresis torque was 10% of the viscous damping torque at the rated motor condition. The motor load power was determined as in Eq. A-12.

$$P_L^r = \tau_L^r \omega_m^r \tag{A-12}$$

where ω_m^r is the rated motor speed. With the ratio of peak power to maximum continuous power known, the torque load, τ_L^r, is solved for at the rated condition. The rated input power was set equal to the motor load power with an assumed power conversion efficiency of 96% as in Eq. A-13

$$P_I^r = \frac{P_L^r}{\eta_m^r} \tag{A-13}$$

The rated input power is recast as motor active power which is a function of the stator voltages and currents as in Eq. A-14.

$$P_I^r = \frac{3}{2}V_q^r I_q^r + \frac{3}{2}V_d^r I_d^r \tag{A-14}$$

Casting input power as active power allows for changes to efficiency as a function of motor temperature to be directly computed.

It is assumed that load power, friction and hysteresis losses subtracted from input power is equal to heating losses. The winding losses were determined as in Eq. A-15.

$$P_H^r = P_I^r - P_L^r - \tau_l^r \omega_m^r \triangleq \frac{3}{2}R_s^r \left(I_q^r\right)^2 \tag{A-15}$$

The rated stator resistance was computed by substituting power terms from Eqs. A-11–A-13 into Eq. A-15. Solving for rated stator resistance resulted in Eq. A-16.

$$R_s^r = \frac{2}{3}\frac{P_H^r}{(I_q^r)^2} \tag{A-16}$$

The rated flux linkage was computed by substituting Eqs. A-2 and A-3 into Eq. A-1. The result is substituted into Eq. A-4 which was used to form Eq. A-17, where the inequality constraint has been converted to an equality at the rated motor condition.

$$G_{inv}V_m^r = \sqrt{(R_s^r I_q^r + \lambda^r n_p \omega_m^r)^2 + (-L_q^r I_q^r n_p \omega_m^r)^2} \tag{A-17}$$

Equation A-17 is crucial in this paper to sizing motor coefficients. The rated battery motor voltage, V_m^r, is defined as the DC-rating provided by motor manufacturers when providing a motor map. Like the number of pole pairs of the motor, an independent choice must be made on the rated motor voltage. The map itself will not change with the choice, but the reasonableness of the resulting motor coefficients are affected by the choice of V_m^r. For this research, 650 V was chosen for V_m^r. The pole pair count, n_p, was set equal to six in the motor coefficient sizing procedure. Other choices could be acceptable depending on desired speed range of the motor; a lower number of pole pairs is more ideal for high-speed applications. Inductance, resistance, and current computed respectively from Equations A-9, A-10 and A-15 were directly substituted into Eq. A-17. The rated flux linkage is solved for as in Eq. A-18.

$$\lambda^r = \frac{V_m^r G_{inv}}{n_p\sqrt{\left[1+\tan^2(\cos^{-1}\Phi)\right]\omega_m^{r\,2} + 2\omega_m^r \frac{P_H^r}{\tau_I} + \left(\frac{P_H^r}{\tau_I}\right)^2}} \tag{A-18}$$

To solve Eq. A-18, the power factor and speed are iteratively changed until convergence in the rated speed is achieved equal to the NDARC rated speed. With power factor, flux linkage, and rated current determined, the rated inductance from Eq. A-9 can be computed.

Rated motor coefficients change with temperature. For generation of motor maps, a lumped mass temperature model from Appendix A in Ref. 25 was utilized to capture variation of the motor coefficients with temperature. For simplicity the coolant temperature was assumed to be held constant at 60 °C. The rated temperature was assumed to be 140 °C, consistent with material properties assumed in the assumed thermal model. Because NDARC produces motor models with

higher maximum continuous power than the experimentally fit motor of 46 hp in Ref. 25, thermal parameters from an experimentally derived thermal model of a 82 hp motor (Ref. 26) was utilized. The area of contact contributing to all thermal resistances was scaled up by a linear factor until the average rated winding temperature of the motor converged to 140 °C in time domain simulations. The temperature model allowed insight into the trend of motor winding and rotor temperatures under specific motor loads. The thermal modeling efforts did not include a model of changes to self-inductance due to temperature. The flux linkage change with temperature was modeled as in Eq. A-19

$$\lambda = \lambda^{20}\left(1+\alpha_{\text{pm}}\left(\theta_r - 20\right)\right) \tag{A-19}$$

where λ^{20} is the flux linkage measured at 20 °C, α_{pm} is the thermal coefficient for permanent magnet material set to -0.001, and θ_r is the average temperature of the motor rotor permanent magnets. The sized flux linkage coefficient is used to solve for λ^{20} when the average winding temperature θ_w is equal to 140 °C from a time domain simulation at the rated condition and θ_r has moved to its steady state temperature typically near 90 °C.

The stator resistance was modeled as in Eq. A-20

$$R_s = R_s^{25}\left(1+\alpha_c\left(\theta_w - 25\right)\right) \tag{A-20}$$

where R_s^{25} is the stator resistance measured at 25 °C, α_c is the copper coefficient set to 3.93×10^{-3}. The R_s^{25} term is solved for by setting the left-hand side of Eq. A-20 to the sized stator resistance and the average winding temperature is equal to 140 °C from a time domain simulation of the thermal model. The changes in resistance and flux linkage with temperature have a significant impact on the efficiencies computed in the motor map.

Speed and Torque Limits Expressions for the motor speed and torque limits are derived in this subsection. The limits may be computed at each segment of the NDARC mission if the maximum available motor speed and torque can also be computed. The definition of maximum available motor speed and peak torque changes when including or excluding flux-weakening control technology. Solutions to peak motor speed and torque were presented with and without flux-weakening control. By rearranging Eq. A-17 and inserting battery voltage, the peak motor speed for any load torque up to the peak load torque can be computed for motors which do not use flux-weakening control. The peak motor speed is defined in Eq. A-21

$$\omega_m^p = \frac{-R_s I_q \lambda + \sqrt{G_{\text{inv}}^2 V_b^2\left(\lambda^2 + L_q^2 I_q^2\right) - L_q^2 I_q^2 R_s^2 I_q^2}}{n_p\left(\lambda^2 + L_q^2 I_q^2\right)} \tag{A-21}$$

where

$$I_q = \frac{2}{3}\frac{\left(\tau_L + \tau_h + c_\mu \omega_m^p\right)}{\lambda n_p} \tag{A-22}$$

The rated superscript was dropped from motor coefficients, to account for possible changes of the flux linkage and inductance due to temperature and current draw at different motor conditions. However, when plotting the boundaries of the motor maps and determining peak conditions, the rated coefficients were used for simplicity. The rated motor constants were substituted into Eq. A-21 for a reasonable peak speed calculation. Since current is a function of speed, Eqs. A-21 and A-22 were easiest to solve by iteratively varying ω_m^p.

It was assumed that peak torque in the flux-weakening region could be allowed to remain constant between the base speed and rated speed. This assumption may be supported with a combination of a higher battery voltage than the rated motor voltage and flux-weakening control. The assumption results in the peak power to continue climbing between the base speed and rated speed. After the rated speed, the power was assumed to level off to a constant value with increasing motor speed. The assumption requires torque to fall to maintain a constant power relationship after the rated speed. The researchers assumed this would be accomplished with flux-weakening control technology fully engaged at the rated speed. To model the impact of flux-weakening control technology past the rated speed, the peak speed was defined as in Eq. A-23

$$\omega_m^p \triangleq \frac{\omega_m^r \tau_L^b}{\tau_L} \le \omega_m^{\text{nl}} \tag{A-23}$$

where ω_m^{nl} is the no-load speed and τ_L^b is the peak load torque achievable at the base speed.

The base speed of the motor, ω_m^b, is defined only at the motor's rated DC voltage and peak power condition. The base speed solution, provided by NDARC, may be computed as in Eq. A-24

$$\omega_m^b = \frac{P_L^p}{\tau_L^b} \tag{A-24}$$

where τ_L^b is the peak load torque at the base speed and P_L^p is peak load power or what NDARC refers to as MRP. The base speed may be iteratively computed by substituting peak current, I_q^p, defined as in Eq. A-25, as well as the motor's rated DC voltage, V_m^r, into Eq. A-21.

$$I_q^p = \frac{2}{3\lambda n_p}\left[\frac{P_L^p}{\omega_m^b} + \tau_h + c_\mu \omega_m^b\right] \tag{A-25}$$

The no-load speed may also be computed by substituting no-load current, I_q^{nl}, defined as in Eq. A-26, as well as the motor's rated DC voltage, V_m^r, into Eq. A-21 and repeating the same speed iteration until convergence.

$$I_q^{\text{nl}} = \frac{2}{3\lambda n_p}\left[\tau_h + c_\mu \omega_m^b\right] \tag{A-26}$$

The no-load speed, ω_m^{nl}, was crucial to compute and was used as a maximum theoretical motor speed. NDARC did not possess knowledge of the no-load speed and may report motor

designs which can exceed the no-load speed. Exceeding the no-load speed with a significant torque load – while theoretically possible with a larger voltage source and/or flux weakening control – may lead to mechanical damage of the motor.

At every segment of the NDARC mission the aerodynamic rotor speed margin as a function of discharge was computed as in Eq. A-27.

$$\Omega_M = \frac{\omega_m^p}{G_r} - \Omega_0 \tag{A-27}$$

where G_r is the rotor transmission gear ratio, and Ω_0 is the NDARC-derived aerodynamic rotor trim speed for any condition. The speed margin is a useful quantity for RPM controlled vehicles which require aerodynamic rotor speed changes to control the vehicle.

The peak load torque driven at any condition depends on the speed of the motor. Equation A-17 is solved for peak load torque as a function of motor speed. The physical solution of the resulting quadratic equation solved for peak load torque was derived as in Eq. A-28.

$$\begin{aligned} &\tau_L^p = -\tau_l \\ &-\frac{3\lambda n_p \left[R_s \lambda n_p \omega_m - \sqrt{G_{\text{inv}}^2 V_b^2 \left(R_s^2 + L_q^2 n_p^2 \omega_m^2\right) - L_q^2 n_p^4 \omega_m^4 \lambda^2}\right]}{2\left(R_s^2 + L_q^2 n_p^2 \omega_m^2\right)} \\ &\qquad\qquad \leq \tau_L^p \end{aligned} \tag{A-28}$$

subject to the constraints

$$\omega_m^b \leq \omega_m \leq \omega_m^{\text{nl}}$$

The peak load torque as provided by a motor manufacturer spec sheet is not likely to be exceeded, even if enough battery voltage has been provided to allow the possibility of peak torque exceedance. The peak load torque constraint, τ_L^p, provided in Eq. A-28 bounds the torque at relevant speeds. The peak load torque is relevant at the base speed of the motor.

When motor speed operations occur after the rated speed, the peak load torque is defined assuming flux weakening control as in Eq. A-29

$$\tau_L^p \triangleq \begin{cases} \tau_L^b, & \omega_m \leq \omega_m^r \\ \dfrac{\omega_m^r \tau_L^b}{\omega_m}, & \omega_m^r < \omega_m < \omega_m^{\text{nl}} \end{cases} \tag{A-29}$$

The aerodynamic rotor torque margin for any flight condition specified in NDARC was computed as in Eq. A-30.

$$Q_M = G_r \tau_L^p - Q_0 \tag{A-30}$$

It was determined during the sizing process, that it would be beneficial to extend the motor map to account for inverter flux-weakening control technology (Ref. 24) and a larger voltage source than the rated motor voltage. Three motor map assumptions were made here. The first assumption was to allow load torque to be held constant between the base speed and rated speed which would require a larger battery voltage than the motor rated voltage. The second assumption was to allow the motor to operate past the rated speed with a constant peak power relationship up to the no-load speed. The third assumption was that continuous torque was modeled to fall assuming constant continuous power past the rated speed. The second and third assumptions are more consistent with certain flux-weakening integrated motor manufacturer specification sheets. A combination of a larger battery voltage than the rated voltage as well as flux-weakening control may be used to achieve constant torque between the base speed and rated speed.

REFERENCES

1. Johnson, W., Silva, C., and Solis, E., "Concept Vehicles for VTOL Air Taxi Operations," Presented at the AHS Technical Conference on Aeromechanics Design for Transformative Vertical Flight, San Francisco, CA, January 16–19, 2018.

2. Silva, C., Johnson, W., Antcliff, K. R., and Patterson, M. D., "VTOL Urban Air Mobility Concept Vehicles for Technology Development," Paper AIAA 2018-3847, 2018 Aviation Technology, Integration, and Operations Conference, AIAA AVIATION Forum, Atlanta, GA, June 25–29, 2018.

3. Johnson, W., "NDARC–NASA Design and Analysis of Rotorcraft," NASA/TP 2015-218751, National Aeronautics and Space Administration, April 2015.

4. Raymer, D. P., *Aircraft Design: A Conceptual Approach*, AIAA, sixth edition, September 2018.

5. Lawrence, B., Theodore, C. R., Johnson, W., and Berger, T., "A Handling Qualities Analysis Tool for Rotorcraft Conceptual Designs," *The Aeronautical Journal*, Vol. 122, (1252), June 2018, pp. 960–987.

6. Chakraborty, I., and Mishra, A. A., "Sizing and Analysis of a Lift-Plus-Cruise Aircraft with Electrified Propulsion," *Journal of Aircraft*, Vol. 60, (3), May–June 2023, pp. 747–765.

7. Hsu, T.-W., Choi, J. J., Amin, D., Tomlin, C., McWherter, S. C., and Piedmonte, M., "Towards Flight Envelope Protection for the NASA Tiltwing eVTOL Flight Mode Transition using Hamilton-Jacobi Reachability," Proceedings of the Vertical Flight Societyś 79th Annual Forum & Technology Display, May 16–18, 2023.

8. Saj, V., Saemi, F., Kamal, T., Wang, Y.-C., Sapra, H., Halder, A., Benedict, M., Kokjohn, S., and Mitsingas, C. M., "A Model-Based Design Framework for Electric VTOL Aircraft," Proceedings of the Vertical Flight Societyś 79th Annual Forum & Technology Display, May 16–18, 2023.

9. Anderson, J. D., *Aircraft Performance and Design*, McGraw-Hill, 1999.

10. Malpica, C., and Withrow-Maser, S., "Handling Qualities Analysis of Blade Pitch and Rotor Speed Controlled eVTOL Quadrotor Concepts for Urban Air Mobility," Proceedings of the VFS International Powered Lift Conference 2020, San Jose, CA, January 21–23, 2020.

11. Withrow-Maser, S., Malpica, C., and Nagami, K., "Multirotor Configuration Trades Informed by Handling Qualities for Urban Air Mobility Application," Proceedings of the Vertical Flight Society's 76th Annual Forum & Technology Display, Virtual, October 6–8, 2020.

12. Withrow-Maser, S., Malpica, C., and Nagami, K., "Impact of Handling Qualities on Motor Sizing for Multirotor Aircraft with Urban Air Mobility Missions," Proceedings of the Vertical Flight Society's 77th Annual Forum, Virtual, May 10–14, 2021.

13. Malpica, C., Withrow-Maser, S., Aires, J., Schuet, S., Suh, P., Barnes, K., Hanson, C., Ruan, A., Altamirano, G., and Foster, J., "Handling Qualities of Multirotor RPM-Controlled Electric-Vertical Take-Off and Landing (eVTOL) Aircraft for Urban Air Mobility (UAM)," Proceedings of the Vertical Flight Societyś 79th Annual Forum & Technology Display, May 16–18, 2023.

14. Schuet, S., Malpica, C., Lombaerts, T., Kaneshige, J., Withrow-Maser, S., Hardy, G., and Aires, J., "A Modeling Approach for Handling Qualities and Controls Safety Analysis of Electric Air Taxi Vehicles," Proceedings of the AIAA AVIATION Forum, Modeling and Simulation Technologies Conference, June 15–19, 2020.

15. Schuet, S., Malpica, C., and Aires, J., "A Gaussian Process Enhancement to Linear Parameter Varying Models," Proceedings of the AIAA AVIATION Forum, Modeling and Simulation Technologies Conference, August 2–6, 2021.

16. Altamirano, G. V., Foster, J. V., Malpica, C., and Schuet, S., "Integrated Handling Qualities Safety Analysis For Conceptual Design of Urban Air Mobility Vehicles," Paper AIAA 2022-4012, AIAA AVIATION 2022 Forum, June 27–July 1, 2022.

17. Peters, D., and HaQuang, N., "Dynamic Inflow for Practical Applications," *Journal of the American Helicopter Society*, Vol. 33, (4), October 1988, pp. 64–48.

18. McRuer, D. T., Droste, C. S., Hansman, R. J., Jr., Hess, R. A., LeMaster, D. P., Matthews, S., McDonnell, J. D., McWha, J., Melvin, W. W., and Pew, R. W., *Aviation Safety and Pilot Control: Understanding and Preventing Unfavorable Pilot-Vehicle Interactions*, National Academy Press, 1997.

19. Tischler, M. B., Colbourne, J. D., Morel, M. R., Biezad, D. J., Cheung, K. K., Levine, W. S., and Moldoveanu, V., "A Multidisciplinary Flight Control Development Environment and Its Application to a Helicopter," *IEEE Control Systems Magazine*, Vol. 19, (4), August 1999, pp. 22–33.

20. Anonymous, "Vehicle Management Systems - Flight Control Function, Design, Installation and Test of Piloted Military Aircraft, General Specification For," Aerospace Standard AS94900, SAE International, August 2018.

21. Anon., "Handling Qualities for Military Rotorcraft," Detail Specification MIL-DTL-32742(AR), Department of Defense, March 2023.

22. Duda, H., "Prediction of Pilot-in-the-Loop Oscillations Due to Rate Saturation," *Journal of Guidance, Control, and Dynamics*, Vol. 20, (3), May–June 1997, pp. 581–587.

23. Lee, S. T., Burress, T. A., and Tolbert, L. M., "Power-Factor and Torque Calculation with Consideration of Cross Saturation of the Interior Permanent Magnet Synchronous Motor with Brushless Field Excitation," Proceedings of the 2009 IEEE International Electric Machines and Drives Conference, May 3–6, 2009.

24. Wai, J., and Jahns, T. M., "A New Control Technique for Achieving Wide Constant Power Speed Operation with an Interior PM Alternator Machine," In IEEE Industry Applications Conference, Vol. 2, Chicago, IL, September 30–October 4, 2001.

25. Salyer, Z., *Thermal Models of Electric Powertrain Components for Cooling System Simulation and Design Requirements*, Undergraduate honors thesis, The Ohio State University, Columbus, Ohio, 2019.

26. Rajput, M. N., *Thermal Modeling of Permanent Magnet Synchronous Motor and Inverter*, Master's thesis, Georgia Institute of Technology, May 2016.